Physics in Medicine & Biology

PAPER

Compressed sensing reconstruction of synthetic transmit aperture dataset for volumetric diverging wave imaging

To cite this article: Yinran Chen *et al* 2019 *Phys. Med. Biol.* **64** 025013

IOP Publishing Phys. Med. Biol. 64 (2019) 025013 (16pp) https://doi.org/10.1088/1361-6560/aaf5f1

Physics in Medicine & Biology

IPEM Institute of Physics and Engineering in Medicine

RECEIVED
14 September 2018

REVISED
13 November 2018

ACCEPTED FOR PUBLICATION
4 December 2018

PUBLISHED
10 January 2019

PAPER

Compressed sensing reconstruction of synthetic transmit aperture dataset for volumetric diverging wave imaging

Yinran Chen[1], Jing Liu[1], Julien Grondin[2], Elisa E Konofagou[2,3] and Jianwen Luo[1,4]

[1] Department of Biomedical Engineering, School of Medicine, Tsinghua University, Beijing, People's Republic of China
[2] Department of Biomedical Engineering, Columbia University, New York, NY, United States of America
[3] Department of Radiology, Columbia University, New York, NY, United States of America
[4] Author to whom any correspondence should be addressed.

E-mail: luo_jianwen@tsinghua.edu.cn

Keywords: volumetric ultrasound imaging, compressed sensing, synthetic transmit aperture, high frame rate

Abstract

A high volume rate and high performance ultrasound imaging method based on a matrix array is proposed by using compressed sensing (CS) to reconstruct the complete dataset of synthetic transmit aperture (STA) from three-dimensional (3D) diverging wave transmissions (i.e. 3D CS-STA). Hereto, a series of apodized 3D diverging waves are transmitted from a fixed virtual source, with the *i*th row of a Hadamard matrix taken as the apodization coefficients in the *i*th transmit event. Then CS is used to reconstruct the complete dataset, based on the linear relationship between the backscattered echoes and the complete dataset of 3D STA. Finally, standard STA beamforming is applied on the reconstructed complete dataset to obtain the volumetric image. Four layouts of element numbering for apodizations and transmit numbers of 16, 32 and 64 are investigated through computer simulations and phantom experiments. Furthermore, the proposed 3D CS-STA setups are compared with 3D single-line-transmit (SLT) and 3D diverging wave compounding (DWC). The results show that, (i) 3D CS-STA has competitive lateral resolutions to 3D STA, and their contrast ratios (CRs) and contrast-to-noise ratios (CNRs) approach to those of 3D STA as the number of transmit events increases in noise-free condition. (ii) the tested 3D CS-STA setups show good robustness in complete dataset reconstruction in the presence of different levels of noise. (iii) 3D CS-STA outperforms 3D SLT and 3D DWC. More specifically, the 3D CS-STA setup with 64 transmit events and the Random layout achieves ~31% improvement in lateral resolution, ~14% improvement in ratio of the estimated-to-true cystic areas, a higher volume rate, and competitive CR/CNR when compared with 3D DWC. The results demonstrate that 3D CS-STA has great potential of providing high quality volumetric image with a higher volume rate.

1. Introduction

Three-dimensional (3D) ultrasound imaging has shown promise in bringing new diagnostic information as it provides image of the examined object in an additional dimension when compared with conventional two-dimensional (2D) imaging. The historical development and clinical applications of 3D ultrasound imaging has been reviewed in the literature (Fenster *et al* 2001, Houck *et al* 2005, 2006, Lang *et al* 2006, Gill and Klas 2007, Salgo 2007, Badano *et al* 2011). The state-of-the-art studies of high volume rate 3D ultrasound imaging concentrate on transmit and/or receive beamforming strategies based on a matrix array probe (Jensen *et al* 2013, Provost *et al* 2014, Papadacci *et al* 2017a, 2017b, Petrusca *et al* 2018). However, matrix array based 3D ultrasound imaging suffers from several obstacles, such as the massive elements/channels, a low volume rate, and poor spatial resolutions in the two lateral dimensions, as will be discussed in the following contents.

In the research community, a typical matrix phased array for 3D ultrasound imaging contains 32 × 32 elements, which requires a number of 1024 independent channels for a full-channel transmit and receive (Jensen *et al* 2013, Petrusca *et al* 2018). This setup brings heavy burdens to the back-end system, making it inconvenient in routine applications. To release the stress resulting from the massive channels, sparse array beamforming is

proposed by properly designing the transmit and/or receive apertures with a modest number of elements, in order to eliminate the redundancies in the transmit-receive element combinations (Davidsen *et al* 1994, Lockwood *et al* 1998, Yen *et al* 2000, Austeng and Holm 2002, Inerfield *et al* 2002, Karaman *et al* 2009, Rasmussen and Jensen 2014). However, periodic sparse arrays result in grating lobe artifacts, whereas random sparse arrays distribute the grating lobe energy over the side lobes, thus deteriorating the image quality (Karaman *et al* 2009).

2D echocardiography generally requires imaging down to 150 mm and a frame rate of at least 20 Hz for real-time interpretation, resulting in ~100 transmit events of focused waves (i.e. single-line-transmit, SLT). As for 3D echocardiography, over ten thousand of focused wave transmissions are needed to scan at full line density without parallelization, for which the volume rate is as low as ~0.5 Hz (Ortega *et al* 2016). There are two major solutions to increase the volume rate. The first one is to transmit unfocused/defocused wave with parallel receive beamforming. The second one is to use multi-line-transmit (MLT) beamforming. The former can image the field-of-view (FOV) by transmitting plane/diverging waves, with each wave covering a large region. In particular, spatial coherent compounding is needed in order to avoid too much loss in image quality (Provost *et al* 2014, Gennisson *et al* 2015, Joos *et al* 2017). For example, virtual arrays with 3×3, 5×5 and 9×9 sources for diverging wave compounding (DWC) are proposed to validate high volume rate 3D imaging with improved image quality (Provost *et al* 2014). Alternatively, 3D MLT is performed by transmitting several focused waves in different directions simultaneously, with each beam scanning a respective sub-sector (Denarie *et al* 2013a, Tong *et al* 2013, Ortega *et al* 2016, Chen *et al* 2017). By combining MLT with parallel receive beamforming (i.e. multi-line-acquisition, MLA), the volume rate can be increased by a factor equal to the product of the numbers of MLT and MLA. For example, 9MLT-4MLA and 16MLT-4MLA are recommended, which speed up the acquisition process by a factor of 36 and 64, respectively, in Ortega *et al* (2016).

Another obstacle faced by matrix array based 3D ultrasound imaging is poor spatial resolutions in the two lateral dimensions (i.e. the azimuth and elevation dimensions), due to a small aperture size of around 10 mm $\times$ 10 mm, which is half the size of a conventional phased array (~20 mm width) (Provost *et al* 2014, Petrusca *et al* 2018). In our previous findings (Chen *et al* 2017), the lateral resolutions in the azimuth and elevation dimensions are as low as ~9 mm at a depth of 110 mm for 9×9 DWC (i.e. DWC with 9×9 virtual sources for compounding), and ~7 mm for 3D SLT at the same depth in simulations. One of the solutions to improve lateral resolution is synthetic transmit aperture (STA) imaging, where individual element sequentially transmits and full aperture receives (Jensen *et al* 2006, Rasmussen and Jensen 2014). High-resolution image is obtained by coherently summing the low-resolution images from the corresponding individual transmit elements, thus dynamic focusing in both transmit and receive is achieved. However, in addition to the poor signal-to-noise ratio (SNR) due to single-element transmit, directly extending STA to matrix array is unrealistic as too many transmit events should be performed, resulting in a very low volume rate. A possible solution is to combine STA with the sparse array technique in order to reduce the number of transmit events while approximating an equivalent effective aperture (Karaman *et al* 2009, Rasmussen and Jensen 2014).

The advantages of STA (e.g. high spatial resolutions) have drawn the attention of researchers by decomposing the backscattered echoes acquired from other beamforming methods into their constituent components, i.e. the complete dataset of STA (single-element transmits and full aperture receives). For example, a novel method is proposed to isolate the contributions of individual transmit elements from a set of focused wave transmissions, recovering the complete dataset of STA, and thus the image quality outside the focal region is also improved (Bottenus 2018). Other strategies include using compressed sensing (CS) to reconstruct high-quality images. CS has been applied to other medical imaging modalities, including magnetic resonance imaging (Lustig *et al* 2007), computed tomography (Chen *et al* 2008) and photoacoustic tomography (Arridge *et al* 2016, Haltmeier *et al* 2016, 2018). In ultrasound imaging, we previously developed a method named CS based STA (CS-STA), which applies CS reconstruction to recover the complete dataset of STA from the backscattered echoes acquired from a series of randomly apodized plane waves on a linear array (Liu *et al* 2017), or randomly apodized diverging waves on a convex array (Liu *et al* 2018). Recently, CS-STA is also demonstrated to be feasible for phased array imaging by transmitting Hadamard-encoded diverging waves and compensating the transmit delays (Liu and Luo 2018). The Hadamard matrices with an order of 2^n ($2 \leqslant n \in N$) can be derived by the following formula (Tiran *et al* 2015):

$$H_2^n = \begin{bmatrix} H_2^{n-1} & H_2^{n-1} \\ H_2^{n-1} & -H_2^{n-1} \end{bmatrix}, H_2 = \begin{bmatrix} 1 & 1 \\ 1 & -1 \end{bmatrix}. \quad (1)$$

One property of these matrices is that their inverse and transpose matrices are the same. As a result, they have been applied to encoding and decoding of some advanced ultrasound beamforming methods (Misaridis and Jensen 2005, Tiran *et al* 2015, Gong *et al* 2017). The CS-STA is demonstrated to be able to provide higher frame rate, higher contrast-to-noise ratio (CNR), higher SNR and competitive spatial resolutions when compared with standard STA. Given that a matrix array can be considered as a 2D phased array, CS-STA may have potential and

good capability for high performance 3D ultrasound imaging with a small number of transmit events. However, no previous attempts have been made to apply CS-STA to 3D imaging.

Therefore, the objective of this paper is to investigate the feasibility of CS-STA on a matrix array, in order to obtain 3D image with a high volume rate and competitive image quality. Furthermore, a periodic sparse array is combined with 3D CS-STA in order to reduce the data storage and computation burdens. More specifically, a series of Hadamard-apodized 3D diverging waves are transmitted from a fixed virtual source located behind the matrix array. Then the backscattered echoes are acquired and CS is used to reconstruct the complete dataset of STA, based on the linear relationship between the backscattered echoes of 3D STA and those of apodized diverging waves. Finally, standard STA beamforming is applied to the reconstructed complete dataset to obtain the final volumetric image.

This paper is organized as follows. In section 2, the transmit scheme and data reconstruction strategy are described. In sections 3 and 4, simulations of the point scatterers and cystic phantom are presented to validate the feasibility and performance of 3D CS-STA. Then the proposed 3D CS-STA setups are compared with 3D SLT and 3D DWC in section 5. Section 6 shows the results of preliminary phantom experiments. Sections 7 and 8 discuss and conclude this work, respectively.

2. Transmit scheme and dataset reconstruction

2.1. Principle of 3D CS-STA

The flow diagram of 3D CS-STA is presented in figure 1(d). It is performed by firstly transmitting a series of apodized 3D diverging waves from a fixed virtual source located behind the matrix array (i.e. with negative axial coordinate), as illustrated in figure 1(a). The backscattered echoes $p_{3D\_DW}(k,j,t)$ received by the jth element in the kth transmit event at time t can be expressed as Liu *et al* (2017):

$$p_{3D\_DW}(k,j,t) = \sum_{i=1}^{M\times N} a_{tx}(k,i) \times e\left(t - \frac{|\overrightarrow{r_i}|}{c} - \frac{|\overrightarrow{r_j}|}{c} - \tau(i)\right) \tag{2}$$

where $a_{tx}(k,i)$ is the transmit apodization coefficient applied to the ith element in the kth transmit event. M and N are the numbers of elements in the azimuth and elevation dimensions, respectively (generally $M = N$). $e(t)$ is the pulse-echo response signal. $\frac{|\overrightarrow{r_i}|}{c} + \frac{|\overrightarrow{r_j}|}{c}$ is the time-of-flight that the pulse transmitted from the ith element, backscattered by the target, and received by the jth element. $\tau(i)$ is the transmit time delay of the ith element in each transmit event. The 3D diverging waves are transmitted from a fixed virtual source, so the transmit delays $\tau(i)$ applied on each element are not changed during transmission.

The objective of 3D CS-STA is to reconstruct the complete dataset of 3D STA from the backscattered echoes. For 3D STA, the backscattered echoes transmitted from the ith element and received by the jth element at time t can be expressed as Liu *et al* (2017):

$$p_{3D\_STA}(i,j,t) = e\left(t - \frac{|\overrightarrow{r_i}|}{c} - \frac{|\overrightarrow{r_j}|}{c}\right). \tag{3}$$

By comparing (2) and (3), the relationship between the backscattered echoes of apodized 3D diverging waves and the complete dataset of 3D STA to be reconstructed is obtained as:

$$p_{3D\_DW}(k,j,t_n) = \sum_{i=1}^{M\times N} a_{tx}(k,i) \times p_{3D\_STA}(i,j,t_n - \tau_n(i)) \tag{4}$$

where the time t is discretized to t_n.

According to (4), the backscattered echoes of 3D apodized diverging waves can be expressed as the linear combination of the complete dataset of 3D STA, which are delayed and weighted by corresponding time delays and apodization coefficients in the transmit elements.

Then, by extracting the slow-time signals (i.e. signals from sequential transmits and receives) from both sides in (4), as follows:

$$\mathbf{y} = \begin{bmatrix} y_1 & \dots & y_k & \dots & y_K \end{bmatrix} = \begin{bmatrix} p_{3D\_DW}(1,j,t_n) & \dots & p_{3D\_DW}(K,j,t_n) \end{bmatrix} \tag{5}$$

$$\begin{aligned} \mathbf{x} &= \begin{bmatrix} x_1 & \dots & x_i & \dots & x_{M\times N} \end{bmatrix} \\ &= \begin{bmatrix} p_{3D\_STA}(1,j,t_n - \tau_n(1)) & \dots & p_{3D\_STA}(M\times N,j,t_n - \tau_n(M\times N)) \end{bmatrix}. \end{aligned} \tag{6}$$

We have:

$$\mathbf{y} = \mathbf{\Phi x} \tag{7}$$

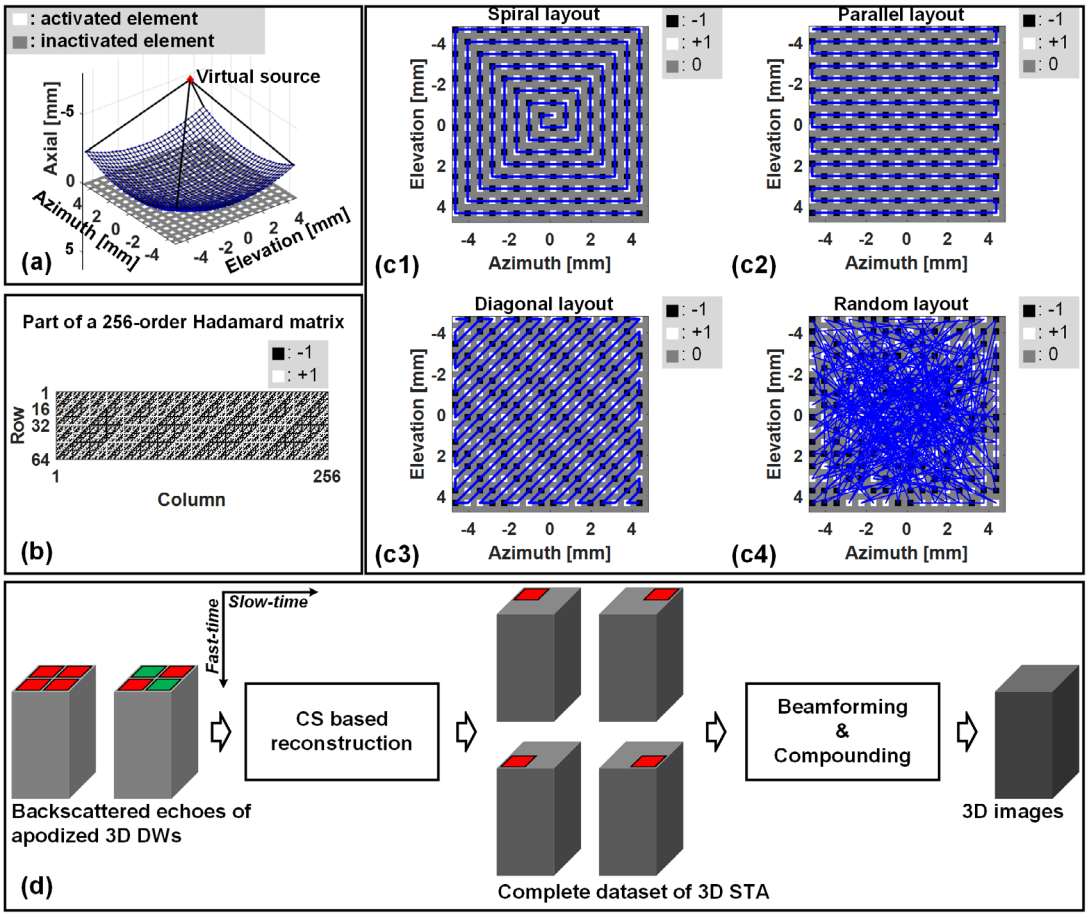

Figure 1. (a) A 3D diverging wave from a virtual source, with opening angles of 60° × 60° in the azimuth and elevation dimensions. The virtual source has negative axial coordinate, while the imaging FOV is in the region with positive axial coordinate. A periodic sparse array of 16 × 16 elements is setup by sub-sampling a typical 32 × 32-element matrix array. The blue dots indicate the time delays applied to the respective elements. (b) Transmit apodization matrix, i.e. the measurement matrix in the CS reconstruction, generated by part of a 256-order Hadamard matrix. The entries on the *i*th row are rearranged into the 16 × 16 elements in the *i*th transmit event. (c1)–(c4) Four apodization layouts for the rearrangement, i.e. spiral, parallel, diagonal and random in the 2nd transmit event, where the apodization coefficients consist of interleaved +1 and −1. The blue lines indicate the path of layouts, i.e. the way to load the row vector of the Hadamard matrix into the 2D array. (d) The flow diagram of 3D CS-STA. The slow-time direction is the direction where the sequential transmits and receives are performed. The fast-time direction is the direction of ultrasound propagation for each transmit/receive event.

$$\mathbf{\Phi} = \begin{pmatrix} a_{tx}(1,1) & \cdots & a_{tx}(1, M \times N) \\ \vdots & \ddots & \vdots \\ a_{tx}(K,1) & \cdots & a_{tx}(K, M \times N) \end{pmatrix} \tag{8}$$

where K is the number of transmits of apodized 3D diverging waves. $M \times N$ is the number of elements in the matrix array, or the number of transmits of 3D STA.

It can be found that (7) is a classical compressive sampling in the CS theory as $K < M \times N$. $\mathbf{\Phi}$ is the measurement matrix. $\mathbf{x}$ has been demonstrated to be sparse when represented in a sparse basis $\mathbf{\Psi}$ in 2D cases (Donoho 2006, Candès and Wakin 2008). Therefore, we have:

$$\mathbf{y} = \mathbf{\Phi}\Psi\mathrm{v} = \mathbf{\Theta}\mathrm{v} \tag{9}$$

where $\mathbf{v} \in \mathbf{R}^{M \times N}$ is the sparse representation of $\mathbf{x}$ and its most entries are approximately zero under a specific tolerated error. In this CS case, the measurement matrix $\mathbf{\Phi}$ and the sparse basis $\mathbf{\Psi}$ should be as incoherent as possible. $\mathbf{v}$ can be reconstructed by solving the following basis pursuit de-noising (BPDN) problem (Van den Berg and Friedlander 2008):

$$\min_{\mathbf{v}} \|\mathbf{v}\|_1 \text{ subject to } \|\mathbf{y} - \mathbf{\Theta}\mathrm{v}\|_2 \leqslant \varepsilon. \tag{10}$$

In this paper, $\mathbf{x}$ is solved by using CS reconstruction algorithms with *sym8* wavelet chosen as the sparse basis $\mathbf{\Psi}$ (Daubechies 1992). The first K rows of an $M \times N$-order Hadamard matrix was selected as the transmit

apodizations (i.e. the measurement matrix $\mathbf{\Phi}$), with entries in the kth row of the matrix rearranged into the $M \times N$ transmit elements in the kth transmit event (Liu and Luo 2018). The SPGL1 solver (Van den Berg and Friedlander 2007, 2008) is used to reconstruct the complete dataset of 3D STA by solving the BPDN problem as formulated in (10).

It should be noted that the reconstructed data, $\mathbf{x}$, have been delayed by the transmit time delays, $\tau_n(i)$. As a result, they should be shifted in the fast-time direction according to $\tau_n(i)$, in order to make the complete dataset of 3D STA aligned for all the transmit elements (Liu and Luo 2018).

Finally, delay-and-sum (DAS) beamforming with dynamic focusing is applied on the complete dataset to reconstruct the final volumetric image, as what is done in conventional 3D STA beamforming.

2.2. Parameter optimization

One of the parameters that should be investigated in the proposed 3D CS-STA is the layout of the transmit apodizations, i.e. the way to rearrange entries in one row of the $M \times N$-order Hadamard matrix into the 2D $M \times N$ aperture. In this study, four layouts, i.e. the Spiral, Parallel, Diagonal, and Random layouts were setup. Figure 1(c) presents the four layouts in the 2nd transmit event, where the corresponding entries in the Hadamard matrix are interleaved by $+1$ and -1.

Another parameter needed to be investigated is the number of transmit events. In this paper, 16, 32 and 64 transmit events were investigated, each of which was in combination with the above four layouts. With a pulse repetition frequency (PRF) of 5 kHz, i.e. an imaging depth of over 150 mm, which is sufficient for imaging of the heart (Papadacci *et al* 2014), the theoretical volume rates were 312, 156 and 78 Hz, respectively.

Furthermore, in this paper, the number of valid transmit and receive channels was reduced to 16×16 (on the basis of a typical 32×32 element matrix array with a 3.0 MHz center frequency and a 0.3 mm pitch), in order to investigate the performance of 3D CS-STA in a modest number of channels, as well as to release the burdens of data storage and computation. The reduction was achieved by selecting the elements with odd indices in the azimuth and elevation dimensions, i.e. a periodic sparse array with an effective pitch being double of that in the dense array, as illustrated in figure 1(a). This configuration of sparse array was chosen in consideration of expanding the array as much as possible to maintain the lateral resolutions, but at the expense of introducing grating lobes.

3. Simulations of point spread functions (PSFs)

3.1. Transducer configuration and beamforming setup

A matrix array of 32×32 elements, 0.3 mm $\times$ 0.3 mm pitch and a center frequency of 3.0 MHz was setup in Field II (Jensen and Svendsen 1992, Jensen 1996). As mentioned in section 2.2, a periodic sparse array with 16×16 elements and 0.6 mm $\times$ 0.6 mm pitch was generated by regularly sub-sampling the corresponding dense array. In transmit beamforming, the virtual source was placed behind the array to generate a 3D diverging wave with full aperture (i.e. 16×16 elements) transmission and opening angles of $60° \times 60°$ in the azimuth and elevation dimensions. The first K ($K = 16, 32, 64$) rows of a 256-order Hadamard matrix was taken as the transmit apodizations, following the rules of the Spiral, Parallel, Diagonal, and Random layouts respectively. In receive, full aperture (i.e. 16×16 elements) was used to record the radio-frequency (RF) backscattered echoes at a sampling frequency of 25 MHz. Then CS reconstruction mentioned in section 2.1 was performed on the backscattered echoes to reconstruct the complete dataset of 3D STA. Finally, standard STA beamforming was used on the complete dataset to reconstruct a pyramidal volume containing 90×90 lines and $60° \times 60°$ opening angles in the azimuth and elevation dimensions. Cross-sections of the azimuth-axial and elevation-axial planes, as well as a C-plane view at a certain depth were displayed for better interpretation of the results.

3.2. Imaged object and quantitative analysis

Four point scatterers located on the axial axis at depths from 20 to 110 mm, with an equal space of 30 mm were imaged to study the characteristic of PSFs. The results of 3D STA with the 16×16-element periodic sparse array (with 256 transmit events required) were taken as benchmark. The PSF of 3D STA from a C-plane view at a depth of 50 mm is given in figure 2(a), with red and blue lines indicating the -6 dB and -55 dB contours, showing the region of main lobe and part of the side lobes, respectively. As a result, the lateral resolutions (LRs) were defined as the diameters of the red contour in the azimuth and elevation dimensions, i.e. the full-width-at-half-maximum (FWHM) of the main lobe. The mean-side-lobe-level (MSLL) was defined as the average value of the side lobes, i.e. region outside the main lobe (Chen *et al* 2017).

3.3. Results of PSFs

The PSFs of 3D STA in a C-plane view at a depth of 50 mm, as well as the views in the azimuth-axial and elevation-axial planes are presented in figures 2(a) and (b1), shown as benchmark. Figures 2(b2) and (b3) show the PSFs

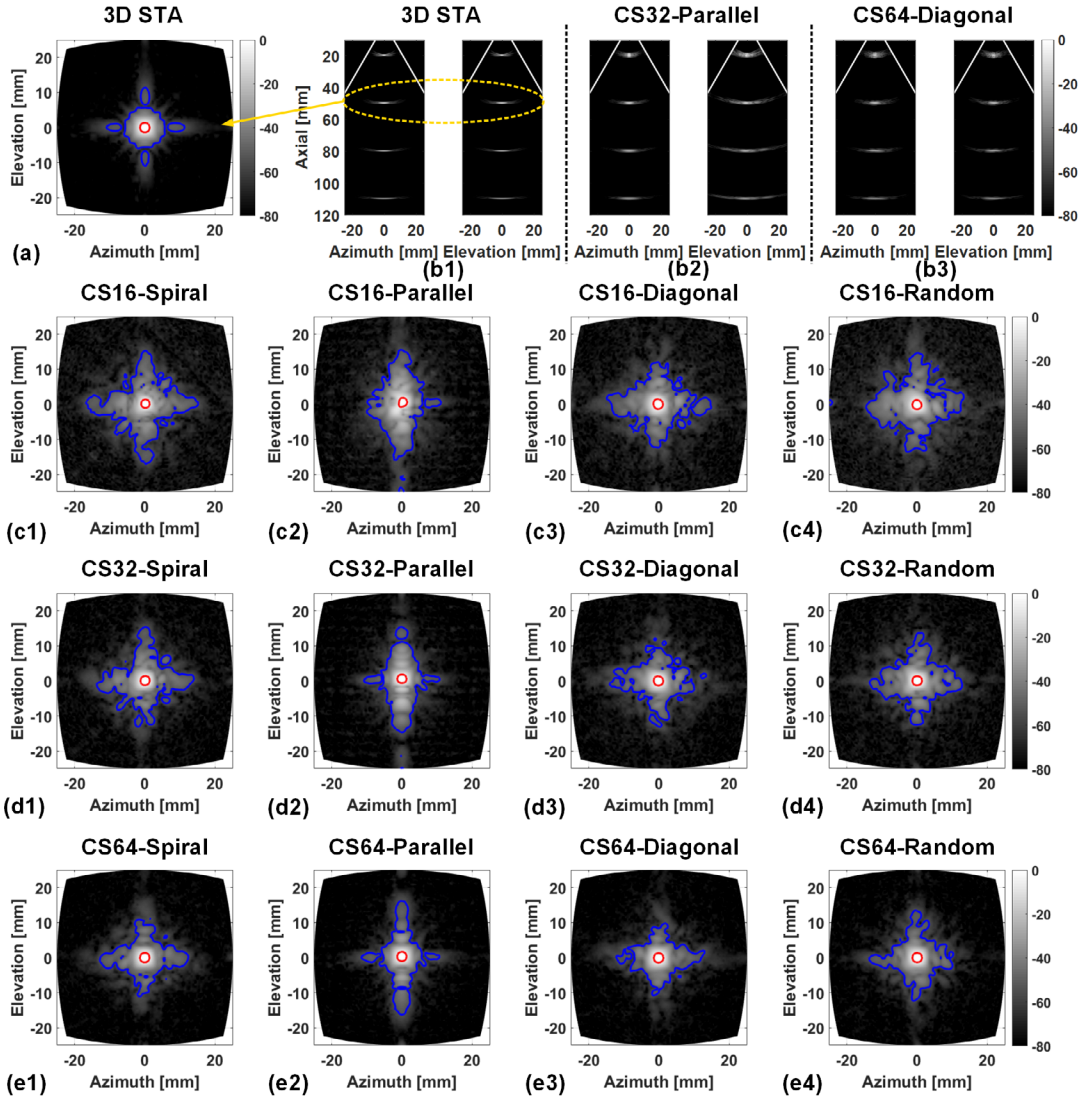

Figure 2. Results of point spread functions (PSFs). The *C*-plane views at a depth of 50 mm are shown. The lines in red and blue indicate the −6 dB and −55 dB contours, respectively. The display dynamic range is 80 dB for better visualization of the side lobes. (a) PSF of standard 3D STA from a *C*-plane view. (b1) PSFs of 3D STA in the azimuth-axial and elevation-axial planes. (b2) and (b3) PSFs of the CS32-parallel and CS64-diagonal setups in the azimuth-axial and elevation-axial planes. (c1)–(c4) PSFs of 3D CS-STA with 16 transmit events, with (c1)–(c4) corresponding to the spiral, parallel, diagonal and random layouts, respectively. (d1)–(d4) PSFs of 3D CS-STA with 32 transmit events and different layouts. (e1)–(e4) PSFs of 3D CS-STA with 64 transmit events and different layouts.

of two 3D CS-STA setups: CS32-Parallel (i.e. 3D CS-STA with 32 transmit events and the Parallel layout) and CS64-Diagonal in the two orthogonal dimensions, respectively. In figures 2(b2) and (b3), increased range lobes and artifacts are found in the axial direction, particularly in the near field (i.e. at a depth of 20 mm). The PSFs of 3D CS-STA from a *C*-plane view at 50 mm depth, obtained from the imaging setups with 16, 32 and 64 transmit events are presented in figures 2(c)–(e), respectively, with the 1st column to the 4th column showing the PSFs of the Spiral, Parallel, Diagonal, and Random layouts, respectively. There are little differences on the main lobes for the tested setups. The side lobes are qualitatively improved as the number of transmit events increases. Unbalanced side lobes are found in the Parallel layout. In comparison, the other layouts generally show balanced side lobes in the azimuth and elevation dimensions.

The LRs in the two dimensions and MSLLs are summarized in figures 3(a) and (b), respectively. The 3D CS-STA setups show slight differences in LRs when compared with 3D STA, except that the CS32-Parallel setup outperforms in the elevation dimension. As illustrated in figure 3(b), the MSLLs of the tested setups are getting closer to those of 3D STA as the number of transmit events increases, showing that the Parallel layout has overall the lowest level of side lobe.

The axial profiles of PSFs with 32 transmit events are given in figure 3(c), qualitatively showing that 3D CS-STA has competitive main lobe widths when compared with 3D STA, at the expense of increased range lobes and artifacts in the axial direction.

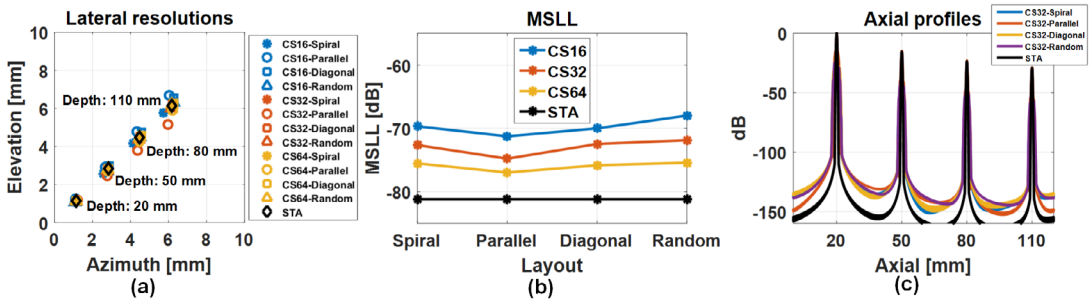

Figure 3. Quantitative results of PSFs. (a) Lateral resolutions (LRs) of the 3D CS-STA setups and 3D STA in the azimuth and elevation dimensions. (b) Mean-side-lobe-levels (MSLLs) of 3D CS-STA and 3D STA. (c) Axial profiles of 3D CS-STA with 32 transmit events, compared with that of 3D STA.

4. Simulations of cystic phantom

4.1. Imaged objects and quantitative analysis

A 30 mm × 30 mm × 40 mm (azimuth × elevation × axial) cubic phantom containing a spherical cystic region with a radius of 10 mm was generated to study the B-mode image characteristics. The scatterers forming this phantom had a density of 5 mm^{-3}, which was sufficient to generate fully developed speckle. Their scattering amplitude was set to 0 inside the cystic region and uniformly distributed between 0 and 1 outside the cystic region. The contrast ratio (CR) and CNR between the cystic region and background were calculated to study the imaging performance (Chen *et al* 2017), as follows:

$$\mathrm{CR} = \mu_{back} - \mu_{cyst} \tag{11}$$

$$\mathrm{CNR} = 20 \times \log_{10}\left(\frac{\mu_{back} - \mu_{cyst}}{\sqrt{\sigma_{back}^2 + \sigma_{cyst}^2}}\right) \tag{12}$$

where μ_{back} and μ_{cyst} are the mean image data (after log-compression) in the background and cystic regions, respectively. And σ_{back} and σ_{cyst} are their respective standard deviations.

Furthermore, to study the robustness of 3D CS-STA in noise conditions, three groups of Gaussian white noise with different levels were generated and added to the backscattered echoes of the tested 3D CS-STA setups and 3D STA. The noise resulted in signal-to-noise ratios (SNRs) of 20, 10, and 0 dB for 3D CS-STA. These noise imitated the electrical noise in real conditions based on the assumption that the energy of electrical noise was independent of the ultrasound signal. The normalized root-mean-square-error (nRMSE) between the reconstructed complete dataset and the noise-free backscattered echoes of 3D STA (i.e. the ground truth) was calculated (Liu *et al* 2017).

4.2. Grating lobe suppression

Due to a periodic sparse array used in this paper, the effective pitch was 0.6 mm in each direction, which was larger than the wavelength of the transmit pulse (i.e. ~0.51 mm for a center frequency of 3.0 MHz). As a result, grating lobe occurred when the steering angle of the received beam exceeded a specific threshold. To mitigate this problem, a method to suppress grating lobe was used by low-pass filtering the received beamformed lines (Hansen *et al* 2009). In 2D imaging case, the cut-off frequency corresponding to the received grating lobe was derived as Hansen *et al* (2009):

$$f_{cut-off} = \frac{c}{(1 + \sin|\theta_{receive}|) \times d} \tag{13}$$

where c, $\theta_{receive}$, and d represented the speed of sound, the receive angle, and the pitch of the array, respectively.

For 3D imaging based on the matrix array, the angular positions of grating lobes, θ_g, were given as Turnbull and Foster (1991):

$$\sin\theta_g = \sin\theta_0 \pm n\lambda/(d\cos\phi_0) \quad n = 1, 2, \ldots \tag{14}$$

where θ_0 and ϕ_0 were the solid angles of the received main lobe in the volume (Turnbull and Foster 1991). While λ and d were the wavelength and pitch, respectively. As a result, the cut-off frequency corresponding to the grating lobe in 3D imaging was derived directly from (13) and (14). In this study, a 7-order Butterworth low-pass infinite impulse response (IIR) filter was applied on the beamformed lines to suppress the grating lobes.

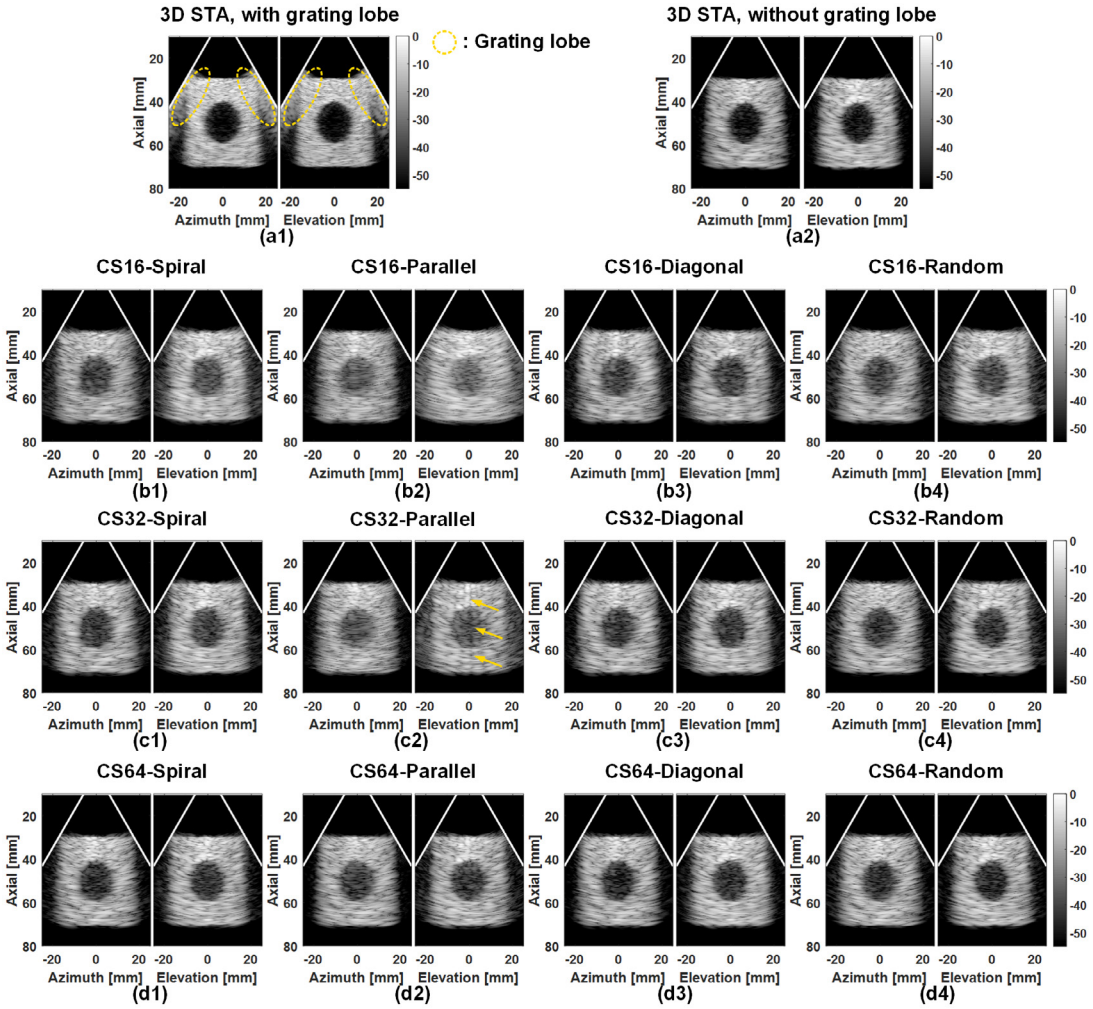

Figure 4. Results of B-mode images of a cystic phantom. The cross-sections of the azimuth-axial and elevation-axial planes are displayed with a 55 dB dynamic range. (a1) Images of 3D STA without suppression of grating lobes. The yellow dashed circles indicate the grating lobes. (a2) Images of 3D STA with suppression of grating lobes, taken as benchmark. (b1)–(b4) Images of the cystic phantom obtained from 3D CS-STA with 16 transmit events, with (b1)–(b4) corresponding to the spiral, parallel, diagonal, and random layouts, respectively. (c1)–(c4) Images obtained from 3D CS-STA with 32 transmit events and different layouts. (d1)–(d4) Images obtained from 3D CS-STA with 64 transmit events and different layouts.

4.3. Results of cystic phantom

The noise-free B-mode images obtained from 3D STA without and with grating lobe suppression are presented in figures 4(a1) and (a2), respectively, showing a significant reduction in grating lobes at the expense of slightly increase of noise inside the cystic region. The B-mode images with grating lobe suppression, obtained from 3D CS-STA with 16, 32, and 64 transmit events are given in figures 4(b)–(d), respectively. Improvements of imaging performance are observed as the number of transmit events increases. However, unbalanced image qualities in the azimuth and elevation dimensions can be found in the Parallel layout, as illustrated in figures 4(b2)–(d2), which is consistent with the results of PSFs. Moreover, gap-like artifacts in the axial direction occur in the elevation dimension of the CS32-Parallel setup, as indicated in figure 4(c2). Otherwise, no significant differences are found qualitatively in the Spiral, Diagonal, and Random layouts with the same number of transmit events.

The B-mode images at the presence of different levels of noise are presented in figure 5, with figures 5(a)–(c) showing the results of 3D STA, CS32-Diagonal, and CS64-Random, respectively. The tested two 3D CS-STA setups both show a significant improvement in image contrast qualitatively when compared with 3D STA under the same noise level. Particularly, at the SNR of 0 dB, the cystic phantom of 3D STA is nearly invisible, while it is still distinguishable in the two 3D CS-STA setups, as illustrated in figures 5(a3)–(c3).

The CRs and CNRs of the cystic region, and the nRMSEs of the reconstructed complete dataset, both without and with noise, are summarized in figure 6. In noise-free condition, the CR, CNR, and nRMSE of 3D CS-STA are improved and getting closer to those of 3D STA as the number of transmit events increases. The Parallel layout shows the worst performance in terms of CR and CNR. The Spiral and Diagonal layouts have very similar performance, while the CR and CNR of the Random layout varies when compared with the Spiral and Diagonal layouts. In terms of nRMSE in noise-free condition, the Diagonal layout has overall the best performance with 32 and 64

transmit events. When different levels of noise are presented, the CR and CNR of 3D STA decrease significantly, while those of 3D CS-STA show slight decline as the level of noise increases. The nRMSEs of the tested 3D CS-STA setups increase as the level of noise increases.

5. Comparison with other 3D imaging methods

5.1. Tested imaging methods for comparison

Three 3D imaging methods were simulated for comparison with 3D CS-STA, i.e. 3D SLT, 5 × 5 DWC (i.e. 3D DWC with 5 × 5 virtual sources) and 9 × 9 DWC. For 3D SLT, the focused points were evenly distributed on a spherical surface centered at the center of the matrix array with a radius of 50 mm, leading to a total number of 8, 100 (i.e. 90 × 90) transmit events and a volume rate of ~0.6 Hz. Please note that the transmit and receive of 3D SLT were both performed on the 32 × 32 element dense array to avoid transmit grating lobes. 3D DWC was setup by placing the virtual sources behind the matrix array, with each virtual source corresponding to a transmit sub-aperture of 8 × 8 valid elements in the periodic sparse array and generating a 3D diverging wave with 60° × 60° opening angles. Full aperture (i.e. 16 × 16 valid elements) were used in receive of 3D DWC. The number of transmit events for 5 × 5 and 9 × 9 DWC were 25 and 81, thus resulting in volume rates of 200 and ~61 Hz, respectively. Furthermore, the same method for grating lobe suppression mentioned in section 4.2 was applied to 5 × 5 and 9 × 9 DWC.

The same point scatterers and cystic phantom as mentioned above were imaged for comparison. The images of the cystic phantom with 3D SLT was not simulated as it was very time consuming. Noise with 10 dB SNR was added to the backscattered echoes of 3D CS-STA and 3D DWC in imaging of the cystic phantom. The LRs of the point scatterers in the azimuth and elevation dimensions, as well as the CR and CNR of the cystic region were quantified for comparison. Furthermore, in order to evaluate the detectability of the cystic region, the area ratio between the estimated cyst and the true cyst was computed (Varnosfaderani *et al* 2018), with the estimated cyst defined as the region where the gray scale values inside the true cystic region (indicated by the black circle) were under a threshold of −30 dB, as illustrated in figure 8(a).

5.2. Results

The PSFs of 3D SLT, 5 × 5 DWC, 9 × 9 DWC, CS32-Random and CS64-Random from a *C*-plane view at a depth of 50 mm, with −6 dB and −55 dB contours superimposed on them are presented in figures 7(a)–(e), respectively. The LRs measured in mm in the azimuth and elevation dimensions are summarized in figure 7(f), showing that 3D CS-STA has the same LRs as 3D SLT at the focal depth in both dimensions. However, the two 3D CS-STA setups show overall the best LR performances when compared with 3D SLT, 5 × 5 DWC and 9 × 9 DWC. Meanwhile, the averaged LRs of all the point scatterers measured in degree for the two 3D DWC and two 3D CS-STA setups are summarized in table 1. The two 3D CS-STA setups achieve an improvement of ~31% in LR when compared with the two 3D DWC setups.

The B-mode images of the cystic phantom obtained from CS32-Random, CS64-Random, 5 × 5 DWC and 9 × 9 DWC are presented in figure 8, showing the zoomed-in cystic region. The −30 dB contours (i.e. the green lines) inside the black circles indicate the estimated boundaries of the cystic region, while the black circles indicate the true boundaries of the cystic region. The CRs, CNRs, cystic area ratios, and volume rates of different imaging setups are summarized in table 1. CS32-Random has competitive CR and CNR, and ~7% improvement of cystic area ratio compared with 5 × 5 DWC, at the expense of a lower volume rate. In contrast, CS64-Random shows competitive CR and CNR, a higher cystic area ratio (~14% improvement) and a higher volume rate compared with 9 × 9 DWC.

6. Preliminary phantom experimental validation

6.1. Experimental setup

Preliminary phantom experiments were performed on a Vantage-256 system (Verasonics, Kirkland, USA), controlling a matrix array of 16 × 16 elements and a center frequency of 2.5 MHz, with an inter-element pitch of 0.85 mm and a bandwidth of 50% (Sonic Concepts, Bothell, USA). Images of a multipurpose tissue/cyst ultrasound phantom (Nuclear Associates 84-317, Fluke Biomedical, Cleveland, USA) were acquired. The imaging methods of 3D STA, four 3D CS-STA setups (i.e. CS32-Parallel, CS32-Random, CS64-Parallel and CS64-Random), and two 3D DWC setups with 5 × 5 and 9 × 9 virtual sources were tested for comparison.

6.2. Results

B-mode images of the phantom in the azimuth-axial and elevation-axial cross-sections are presented in figure 9, with the results of 3D STA shown as benchmark in figure 9(g). A group of wire targets with 10 mm spacing are located at the center of the FOV. Two cysts with radii of 2 mm and 4 mm respectively are indicated in figure 9(g).

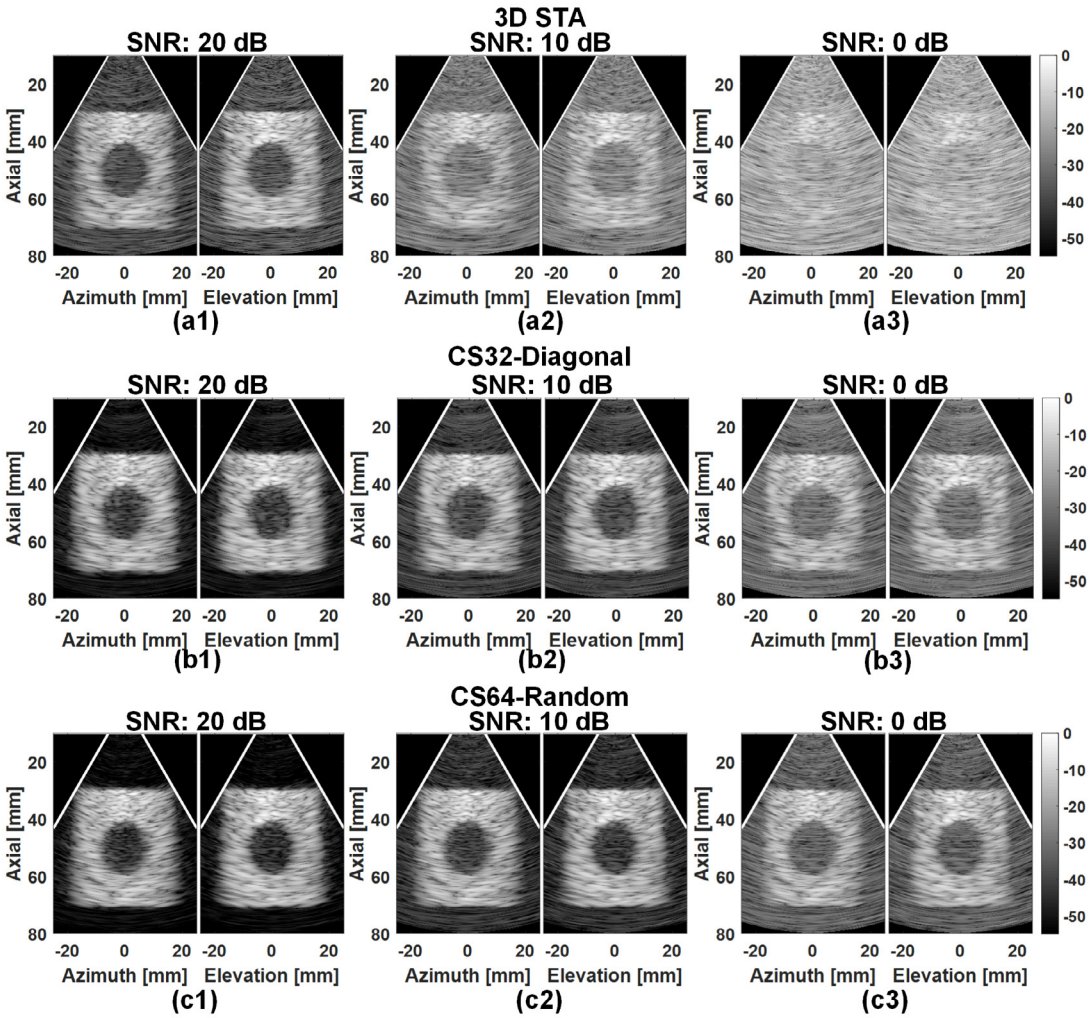

Figure 5. B-mode images of the cystic phantom obtained from 3D STA and two 3D CS-STA setups at the presence of different level of noise. The same level of Gaussian noise was added in the backscattered echoes of 3D STA and 3D CS-STA. (a1)–(a3) Images obtained from 3D STA, with (a1)–(a3) corresponding to SNRs of 20 dB, 10 dB, and 0 dB, respectively. (b1)–(b3) Images obtained from 3D CS-STA with 32 transmit events and the Diagonal layout. (c1)–(c3) Images obtained from 3D CS-STA with 64 transmit events and the Random layout.

Gap-like artifacts can be found in the elevation-axial plane of the two Parallel layouts, as illustrated in figures 9(c) and (d), which are consistent with the simulation results. By qualitative observation, CS32-Random and CS64-Random have better reconstruction of the wire targets when compared with 5 × 5 DWC and 9 × 9 DWC, especially for the targets at depths over 60 mm. The quantitative measurement of the lateral resolutions of the wire targets are summarized in figure 9(h), showing that the two 3D CS-STA setups have similar performance to that of 3D STA. Moreover, they outperform the two 3D DWC setups, which is also consistent with the simulation results.

7. Discussion

7.1. Brief summaries

In this paper, a matrix array based 3D ultrasound imaging method named 3D CS-STA is proposed by: (i) transmitting a series of 3D diverging waves from a fixed virtual source, with the *i*th transmission apodized by rearranging the *i*th row of a Hadamard matrix into the 2D transmit aperture. (ii) Applying CS to reconstruct the complete dataset of 3D STA from the backscattered echoes in the slow-time direction sample-by-sample. (iii) Performing standard 3D STA beamforming on the complete dataset to reconstruct the final volumetric image. Different numbers of transmit events, i.e. 16, 32 and 64, in combination with four transmit apodization layouts, i.e. the Spiral, Parallel, Diagonal, and Random layouts are evaluated. The PSFs demonstrate that 3D CS-STA has competitive LRs when compared with 3D STA. The CR and CNR results of the cystic phantom demonstrate that the Spiral and Diagonal layouts have very similar performances, while the Random layout has varied performance compared with the Spiral and Diagonal layouts. Furthermore, the Parallel layout is not recommended due to unbalanced side lobes in the azimuth and elevation dimensions and the lowest CR/CNR

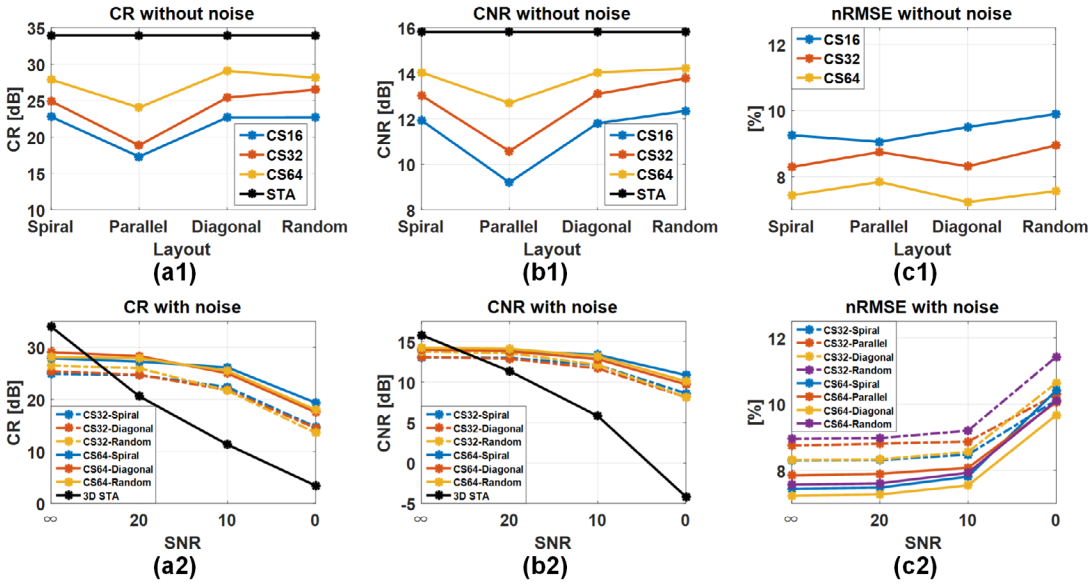

Figure 6. Quantitative results of B-mode images of the cystic phantom. (a1) and (a2) Contrast ratios (CRs) of the cystic region without and with noise, respectively. In noise-free condition, the results of 3D STA is taken as benchmark. Setups of 32 and 64 transmit events, in combination with the spiral, diagonal and random layouts are selected to study their robustness to noise. (b1) and (b2) Contrast-to-noise ratios (CNRs) of the cystic region without and with noise, respectively. (c1) and (c2) Normalized root-mean-square-errors (nRMSEs) of the reconstructed complete dataset of 3D CS-STA compared with 3D STA. (c1) The results in noise-free condition. (c2) The results in the presence of different levels of noise.

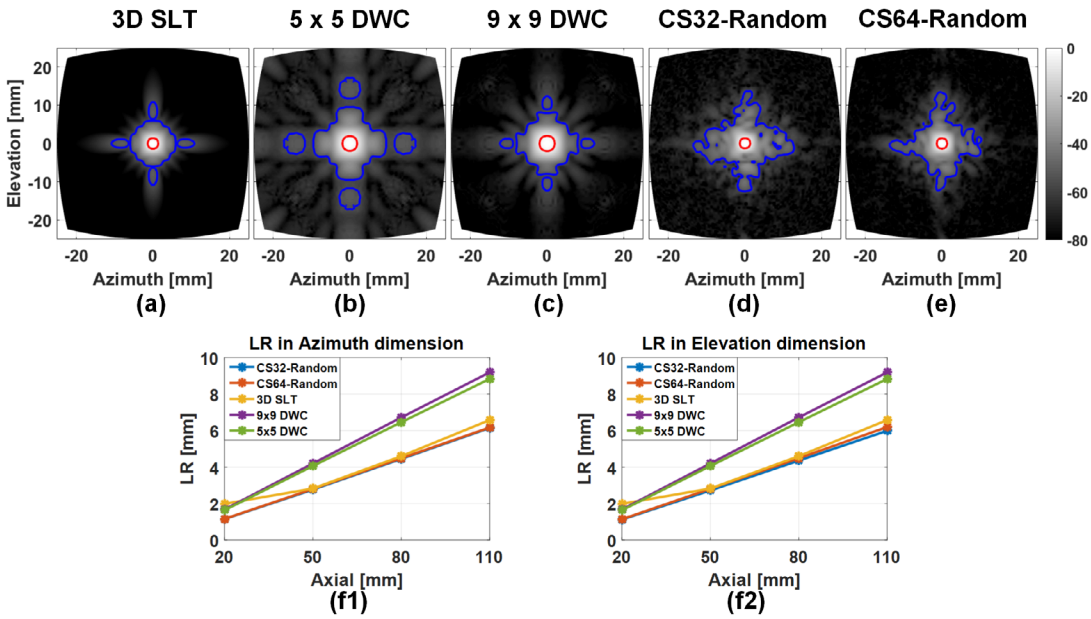

Figure 7. PSF of two 3D CS-STA setups, 3D single-line-transmit (SLT), and 3D diverging wave compounding (DWC) with 5×5 and 9×9 virtual sources. A C-plane view at depth of 50 mm are shown with a dynamic range of 80 dB. The red and blue lines indicate the -6 dB and -55 dB contours, respectively. (a) PSF of 3D SLT, with transmit focus at depth of 50 mm. (b) PSF of 5×5 DWC. (c) PSF of 9×9 DWC. (d) PSF of CS32-random. (e) PSF of CS64-random. (f1) and (f2) LRs of the tested imaging methods in the azimuth and elevation dimensions, respectively.

performance. Furthermore, the robustness of CS reconstruction to noise is measured by the nRMSE, showing that more precise reconstruction is achieved as the number of transmit events increases. When compared with 3D DWC, the proposed 3D CS-STA shows better LR (~31% improvement), higher ratio of the estimated-to-true cystic areas (~14% improvement), and competitive CR/CNR. Finally, preliminary phantom experiments show consistency with the simulations.

The novelty of this paper lies in that we conduct the first try to apply CS-based STA in 3D ultrasound beamforming, which highly meets the requirements of higher lateral resolutions and higher volume rate in 3D imaging. Design of transmit apodization is of great importance in CS-STA, and inappropriate designs of apodization will lead to deteriorated image quality. In particular, in 3D ultrasound beamforming, more attentions should be

Table 1. Quantitative comparison of 3D CS-STA and 3D DWC.

Method	CS32-random	5 × 5 DWC	CS64-random	9 × 9 DWC
Mean LR in azi (°)	3.234 ± 0.008	4.641 ± 0.035	3.271 ± 0.007	4.808 ± 0.013
Mean LR in ele (°)	3.224 ± 0.007	4.641 ± 0.035	3.268 ± 0.001	4.808 ± 0.013
CR (dB)	21.68	21.21	25.49	25.45
CNR (dB)	12.12	11.22	13.17	12.48
Cystic area ratio	0.65	0.61	0.72	0.63
Volume rate (Hz)	156	200	78	61

azi = azimuth dimension, ele = elevation dimension.

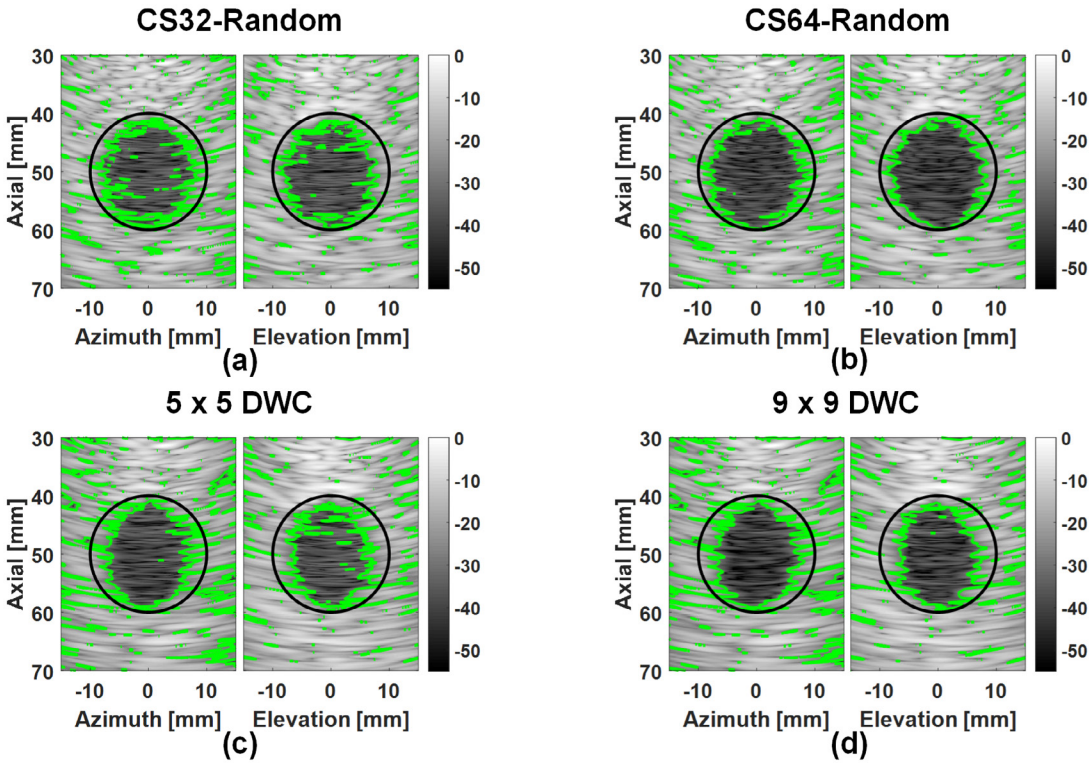

Figure 8. B-mode images of (a) CS32-random, (b) CS64-random, (c) 5 × 5 DWC, and (d) 9 × 9 DWC, respectively. Cross-sections in the azimuth-axial and elevation-axial planes are displayed with a dynamic range of 55 dB. The black circles indicate the boundaries of true cystic region. The green lines indicate the −30 dB contours. The regions surrounded by the −30 dB contours inside the black circles show the estimated cystic targets.

paid in the transmit apodizations due to the additional dimension in the matrix array, compared with the conventional linear array in 2D imaging.

7.2. Selection of transmit apodizations

The transmit apodizations, or the measurement matrix $\mathbf{\Phi}$ in CS reconstruction, is selected to be the first K (i.e. the number of transmit events) rows of a 256-order Hadamard matrix, which is different from what is done in Liu *et al* (2017, 2018), where the apodization coefficients are randomly distributed in the interval of [0, 1] and is in analogy to that in Liu and Luo (2018). Two reasons are taken into consideration when applying this kind of transmit apodizations. Firstly, in terms of SNR, the Hadamard apodizations result in higher energy transmitted into the imaging volume as their amplitudes are either +1 or −1. Secondly, in terms of CS reconstruction, two conditions on the measurement matrix $\mathbf{\Phi}$ are necessary for robust recovery: the restricted isometry property (RIP) and the incoherence between $\mathbf{\Phi}$ and the sparse basis $\mathbf{\Psi}$. RIP indicates that all the subsets of s (i.e. the number of non-zero entries of $\mathbf{v}$) columns taken from $\mathbf{\Theta}$ are nearly orthogonal. An equivalent case is that $\mathbf{\Phi}$ and $\mathbf{\Psi}$ are incoherent (Donoho 2006, Candès and Wakin 2008). The partial Hadamard matrix has been proven to be less incoherent with $\mathbf{\Psi}$ (e.g. *sym8* wavelets) than the random one (Liu and Luo 2018). Furthermore, the first K rows, instead of other row combinations of the Hadamard matrix are chosen in order to maintain the low coherence condition and make the acoustic intensity distribution more homogeneous to avoid the discontinuity artifacts, which has been discussed thoroughly in the previous study (Liu and Luo 2018).

7.3. Layouts of transmit apodizations

Four apodization layouts, i.e. the Spiral, Parallel, Diagonal, and Random layouts are investigated. In the study of PSFs, the Parallel layout shows unbalanced side lobes, while the other layouts do not show much differences, as illustrated in figures 2 and 3(b). However, in the study of the cystic phantom, the CR and CNR performances of the Parallel layout is deteriorated due to unbalanced side lobes, as shown in figures 4 and 6. It is also found that the Spiral, Diagonal, and Random layouts have similar performances in terms of CR and CNR under noise-free condition.

Generally, there are a tremendous number of possible apodization layouts and one or several of them would be the 'optimal' choices. However, going through all the possible layouts is trivial and extremely time-consuming. Moreover, the criteria of the 'optimal' layout is ambiguous. A typical example is the Parallel layout, which obtains contrary performance, i.e. slightly better LR and MSLL in the PSF, but worse CR and CNR in the image of the cystic phantom. As a result, three regular layouts (i.e. Spiral, Parallel, and Diagonal) and a random layout are selected in this paper for preliminary investigation, and the results of the PSFs and cystic phantom have shown that the Parallel layout is not recommended, while the other layouts have obtained acceptable performances.

7.4. Selection of sparse array

In this paper, a periodic sparse array containing 16×16 elements is generated in order to reduce the data storage and computation burdens. The reasons of choosing this sparse array contain two folds. On one hand, the array size should be as large as possible in order to guarantee good lateral resolution, as the lateral beam width is mainly determined by the aperture size. On the other hand, the periodic sparse array is simple to design, thus making it easier for a real experimental implementation. Although this periodic sparse array increases the risk of introducing grating lobes when the beam is steered beyond a specific angle. They can be mostly suppressed by several methods. In this study, low-pass filtering is applied on the beamformed lines to remove the grating lobe components, at the expense of slightly degrading the spatial and contrast resolutions. Other methods for grating lobe suppression include modulation of the receive beams (Ponnle *et al* 2013), use of virtual sub-wavelength receiving elements (Peng and Li 2015, Lin and Li 2016), or calculation of the sign coherence factor as the weighting factor of beamformed data (Torbatian *et al* 2010, 2013).

Other sparse array designs include the use of different cross arrays in transmit and receive (Rasmussen and Jensen 2014), X-shaped, Plus-Shaped, and/or Boundary-shaped in transmit and receive, respectively (Karaman *et al* 2009), or other designs of periodic/random sparse arrays (Davidsen *et al* 1994, Lockwood *et al* 1998, Inerfield *et al* 2002). The proposed 3D CS-STA might perform better when combined with other sparse arrays. However, it is important that 3D CS-STA requires the same apertures in transmit and receive. As a result, the combinations of different sparse array designs in transmit and receive are infeasible for 3D CS-STA. Combining 3D CS-STA with other sparse arrays for better imaging performance is beyond the scope of this paper. However, it is worthwhile to perform more throughout investigation in the future study.

7.5. Comparison with other reconstruction strategies

Another attempt on reconstructing the complete dataset of STA is done by relating the backscattered echoes of a set of focused waves and the complete dataset through an encoding matrix, which consisted of transmitting time delays of respective elements in each transmit event (Bottenus 2018). Data recovery is achieved by directly inversing the encoding matrix in the time or frequency domain. The method proposed in Liu and Luo (2018) and extended in this paper is different from that proposed in Bottenus (2018). The latter reconstructs the complete dataset of STA from the backscattered echoes of focused wave transmissions with different transmit time delays. Thus the overall 2D image quality (especially outside of the focal region), instead of frame rate is improved. In contrast, the method in previous study (Liu and Luo 2018) and in this paper reconstruct the complete dataset of STA from the backscattered echoes of diverging wave transmissions with different apodization coefficients, while the transmit time delays remain the same for different transmit events. This method achieves high image quality with a small number of transmit events.

CS reconstruction of volumetric ultrasound imaging can also be achieved by using dictionary learning and line-wise subsampling (Lorintiu *et al* 2015). In Lorintiu *et al* (2015), volumetric ultrasound image is acquired by a commercial system and sub-sampled by 3D random sampling or 3D line-wise sampling. Then dictionary learning is used to reconstruct high-quality volumetric image from the sub-sampled data. This is based on the image data beamformed with fixed transmit and receive focus, which is different from the proposed 3D CS-STA, where CS reconstruction is performed on the backscattered echoes acquired from 3D diverging waves.

7.6. Limitations

One limitation of this study is that the influence of motion is not taken into consideration. The velocity of the myocardium has been reported to be between 50 mm s^{-1} and 80 mm s^{-1} in systole and lower in diastole (Hazard

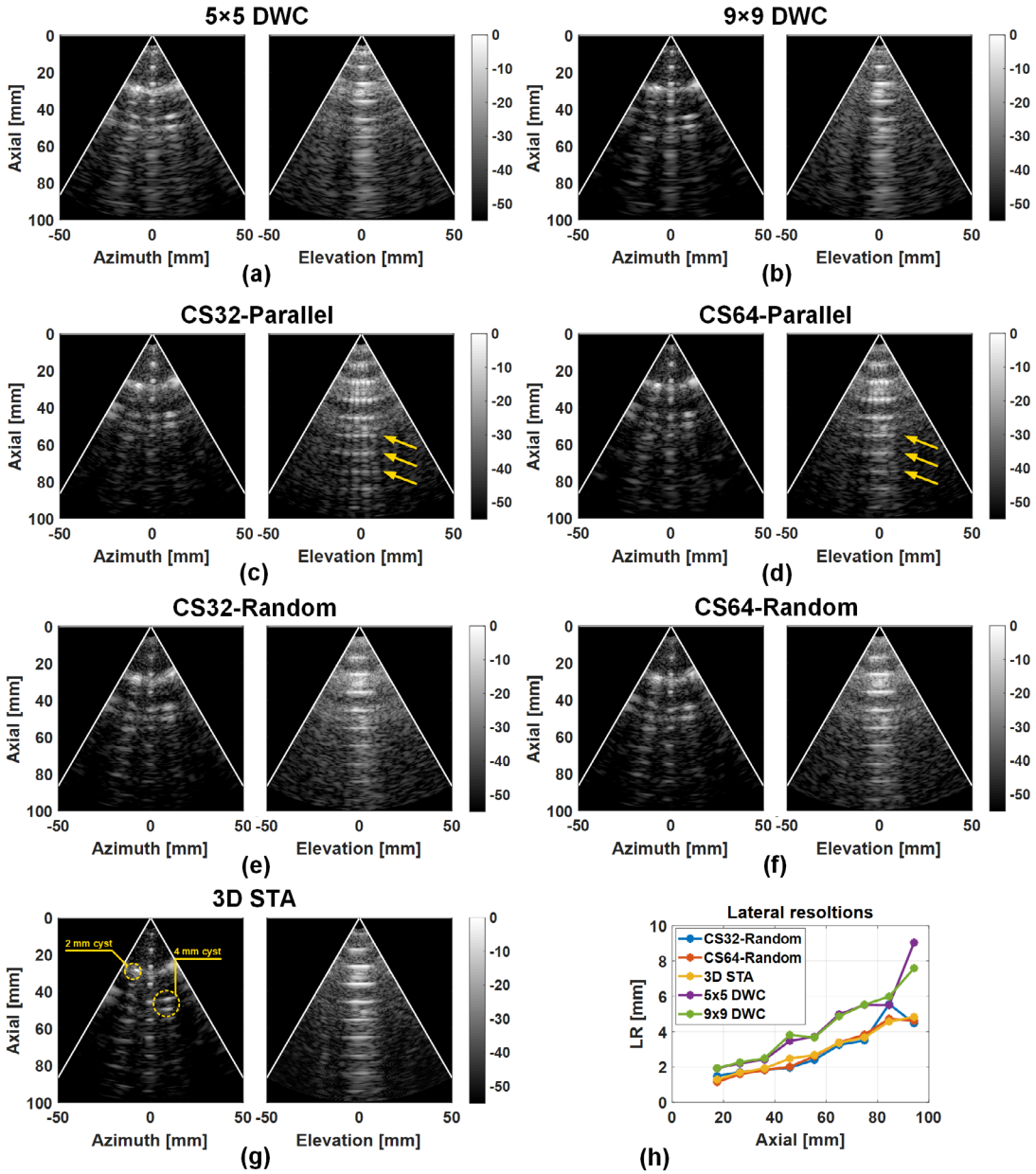

Figure 9. B-mode images of phantom experiments. (a) 5 × 5 DWC, (b) 9 × 9 DWC, (c) CS32-parallel, (d) CS64-parallel, (e) CS32-random, (f) CS64-random, and (g) 3D STA. Cross-sections in the azimuth-axial and elevation-axial planes are displayed with a dynamic range of 55 dB. The wire targets with 10 mm spacing are located in the center of the FOV. Two cystic targets with radius of 2 and 4 mm are indicated in (g). (h) The lateral resolutions of the wire targets of the tested imaging methods.

and Lockwood 1999). In STA and DWC, motion artifacts will be induced in the compounding process due to phase incoherence, showing loss of spatial and contrast resolutions (Wang and Lu 2007, Denarie *et al* 2013b, Gammelmark and Jensen 2014, Chen *et al* 2018). However, it has been demonstrated that lateral motion below 2 m s^{-1}, and axial motion below 80 mm s^{-1} do not significantly change the secondary lobes in the radiation patterns in STA beamforming (Hazard and Lockwood 1999). The influence of motion on CS reconstruction has not been studied yet. The robustness of CS-STA to motion should be fully investigated in the future.

Another limitation is the time-consuming for reconstruction of the complete dataset. In the study of the cystic phantom, the size of the input data to be processed is 3072 × 256 × K (number of samples per channel × number of receive channels × number of transmit events). While the size of the reconstructed complete dataset is 3072 × 256 × 256. It takes the SPGL1 solver around 2.5 h to complete the data reconstruction sample-by-sample in Matlab 2013a (The MathWorks, Inc., Natick, MA, USA) embedded on a PC workstation (Dell Precision Tower 7910, Intel (R) Xeon (R) CPU E5-2670 v3 @ 2.3 GHz, 64 GB RAM). This time duration is far away from real-time implementation. Acceleration could be achieved by quadrature demodulation of the received RF data to reduce the data size, by parallel computation through multi-core CPU or graphics processing unit (GPU), or by combination of the above methods.

8. Conclusion

In this study, high performance volumetric ultrasound imaging is achieved by 3D CS-STA, i.e. recovering the complete dataset of 3D STA from a series of apodized 3D diverging waves through CS reconstruction. Meanwhile, in order to reduce the data storage and computation burdens, a periodic sparse array contained 16 × 16 elements is setup. Four apodization layouts (i.e. Spiral, Parallel, Diagonal, and Random) and three different numbers of transmit events (i.e. 16, 32 and 64) are investigated. Studies of point scatterers and a cystic phantom demonstrate that 3D CS-STA obtains competitive LRs to 3D STA and higher CR/CNR as the number of transmit event increases. Moreover, the Parallel layout results in unbalanced image qualities in the azimuth and elevation dimensions, while the other layouts show similar performances. The robustness of several 3D CS-STA setups in noise conditions is also investigated by calculating nRMSE between the reconstructed complete dataset and that of 3D STA. Furthermore, 3D CS-STA is compared with 3D SLT, 5 × 5 and 9 × 9 DWC. Results of PSFs show that the proposed method has overall better LRs when compared with 3D SLT, and a significant LR improvement of ~31% when compared with 5 × 5 and 9 × 9 DWC. The results of the cystic phantom demonstrate that 3D CS-STA with 64 transmit events and the Random layout obtains a higher area ratio of the cystic region (0.72 versus 0.63), competitive CR/CNR, and a higher volume rate (78 Hz versus 61 Hz) when compared with 9 × 9 DWC. Phantom experiments also showed good correlation with the simulation findings.

Acknowledgments

This study was supported in part by the National Natural Science Foundation of China (NSFC) (61871251, 81471665 and 81561168023) and the National Key R&D Program of China (2016YFC0102200).

ORCID iDs

Yinran Chen https://orcid.org/0000-0001-8062-1859
Jing Liu https://orcid.org/0000-0002-4207-0029
Julien Grondin https://orcid.org/0000-0002-5704-5846
Jianwen Luo https://orcid.org/0000-0001-9215-5568

References

Arridge S, Beard P, Betcke M, Cox B, Huynh N, Lucka F, Ogunlade O and Zhang E 2016 Accelerated high-resolution photoacoustic tomography via compressed sensing *Phys. Med. Biol.* **61** 8908–40

Austeng A and Holm S 2002 Sparse 2D arrays for 3D phased array imaging-design methods *IEEE Trans. Ultrason. Ferroelectr. Freq. Control* **49** 1073–86

Badano L P, Lang R M and Zamorano J L 2011 *Textbook of Real-Time Three Dimensional Echocardiography* (Berlin: Springer)

Bottenus N 2018 Recovery of the complete data set from focused transmit beams *IEEE Trans. Ultrason. Ferroelectr. Freq. Control* **65** 30–8

Candès E J and Wakin M B 2008 An introduction to compressive sampling *IEEE Signal Process. Mag.* **25** 21–30

Chen G H, Tang J and Leng S 2008 Prior image constrained compressed sensing (PICCS): a method to accurately reconstruct dynamic CT images from highly undersampled projection data sets *Med. Phys.* **35** 660–3

Chen Y, D'hooge J and Luo J 2018 Doppler-based motion compensation strategies for 3-D diverging wave compounding and multiplane-transmit beamforming: a simulation study *IEEE Trans. Ultrason. Ferroelectr. Freq. Control* **65** 1631–42

Chen Y, Tong L, Ortega A, Luo J and D'hooge J 2017 Feasibility of multiplane-transmit beamforming for real-time volumetric cardiac imaging: a simulation study *IEEE Trans. Ultrason. Ferroelectr. Freq. Control* **64** 648–59

Daubechies I 1992 *Ten Lectures on Wavelets* (Philadelphia, PA: SIAM) p 61

Davidsen R E, Jensen J A and Smith S W 1994 Two-dimensional random arrays for real time volumetric imaging *Ultrason. Imaging* **16** 143–63

Denarie B, Bjastad T and Torp H 2013a Multi-line transmission in 3D with reduced crosstalk artifacts: a proof of concept study *IEEE Trans. Ultrason. Ferroelectr. Freq. Control* **60** 1708–18

Denarie B, Tangen T A, Ekroll I K, Rolim N, Torp H, Bjåstad T and Lovstakken L 2013b Coherent plane wave compounding for very high frame rate ultrasonography of rapidly moving targets *IEEE Trans. Med. Imaging* **32** 1265–76

Donoho D L 2006 Compressed sensing *IEEE Trans. Inform. Theory* **52** 1289–306

Fenster A, Downey D B and Cardinal H N 2001 Three-dimensional ultrasound imaging *Phys. Med. Biol.* **46** R67

Gammelmark K L and Jensen J A 2014 2D tissue motion compensation of synthetic transmit aperture images *IEEE Trans. Ultrason. Ferroelectr. Freq. Control* **61** 594–610

Gennisson J, Provost J, Deffieux T, Papadacci C, Imbault M, Pernot M and Tanter M 2015 4D ultrafast shear-wave imaging *IEEE Trans. Ultrason. Ferroelectr. Freq. Control* **62** 1059–65

Gill E A and Klas B 2007 Three-dimensional echocardiography: an historical perspective *Cardiol. Clin.* **25** 221–9

Gong P, Song P and Chen S 2017 Ultrafast synthetic transmit aperture imaging (USTA) using Hadamard-encoded virtual sources with overlapping sub-apertures *IEEE Trans. Med. Imaging* **36** 1372–81

Haltmeier M, Berer T, Moon S and Burgholzer P 2016 Compressed sensing and sparsity in photoacoustic tomography *J. Opt.* **18** 1–12

Haltmeier M, Sandbichler M, Berer T, Bauer-Marschallinger J, Burgholzer P and Nguyen L 2018 A sparsification and reconstruction strategy for compressed sensing photoacoustic tomography *J. Acoust. Soc. Am.* **143** 3838–48

Hansen H H, Lopata R G and de Korte C L 2009 Noninvasive carotid strain imaging using angular compounding at large beam steered angles: validation in vessel phantoms *IEEE Trans. Med. Imaging* **28** 872–80

Hazard C and Lockwood G 1999 Effects of motion on a synthetic aperture beamformer for real-time 3D ultrasound *Presented at the Ultrasonics Symp. (IUS), 1999 IEEE Int.* pp 1221–4
Houck R C, Cooke J and Gill E A 2005 Three-dimensional echo: transition from theory to real-time, a technology now ready for prime time *Curr. Probl. Diagn. Radiol.* **34** 85–105
Houck R C, Cooke J and Gill E A 2006 Live 3D echocardiography: a replacement for traditional 2D echocardiography? *AJR Am. J. Roentgenol.* **187** 1092–106
Inerfield M, Lockwood G R and Garverick S L 2002 A sigma-delta-based sparse synthetic aperture beamformer for real-time 3D ultrasound *IEEE Trans. Ultrason. Ferroelectr. Freq. Control* **49** 243–54
Jensen J A 1996 Field: a program for simulating ultrasound systems *10th Nordic-Baltic Conf. on Biomedical Imaging Published in Medical & Biological Engineering & Computing* vol 4 pp 351–3
Jensen J A and Svendsen N B 1992 Calculation of pressure fields from arbitrarily shaped, apodized, and excited ultrasound transducers *IEEE Trans. Ultrason. Ferroelectr. Freq. Control* **39** 262–7
Jensen J A, Holten-Lund M F, Nilsson R T, Hansen M, Larsen U D, Domsten R P, Tomov B G, Stuart M B, Nikolov S I and Pihl M J 2013 SARUS: a synthetic aperture real-time ultrasound system *IEEE Trans. Ultrason. Ferroelectr. Freq. Control* **60** 1838–52
Jensen J A, Nikolov S I, Gammelmark K L and Pedersen M H 2006 Synthetic aperture ultrasound imaging *Ultrasonics* **44** e5–15
Joos P, Liebgott H, Varray F, Petrusca L, Garcia D, Vray D and Nicolas B 2017 High-frame-rate 3D echocardiography based on motion compensation: an *in vitro* evaluation *Presented at the Ultrasonics Symp. (IUS), 2017 IEEE Int.* pp 1–4
Karaman M, Wygant I O, Oralkan Ö and Khuri-Yakub B T 2009 Minimally redundant 2D array designs for 3D medical ultrasound imaging *IEEE Trans. Med. Imaging* **28** 1051–61
Lang R M, Mor-Avi V, Sugeng L, Nieman P S and Sahn D J 2006 Three-dimensional echocardiography: the benefits of the additional dimension *J. Am. Coll. Cardiol.* **48** 2053–69
Lin C-Y and Li M-L 2016 Plane wave imaging using virtual sub-wavelength receiving elements *Presented at the Ultrasonics Symp. (IUS), 2016 IEEE Int.* pp 1–4
Liu J and Luo J 2018 Compressed sensing based synthetic transmit aperture for phased array using Hadamard encoded diverging wave transmissions *IEEE Trans. Ultrason. Ferroelectr. Freq. Control* **65** 1141–52
Liu J, He Q and Luo J 2017 A compressed sensing strategy for synthetic transmit aperture ultrasound imaging *IEEE Trans. Med. Imaging* **36** 878–91
Liu J, He Q and Luo J 2018 Compressed sensing based synthetic transmit aperture imaging: validation in a convex array configuration *IEEE Trans. Ultrason. Ferroelectr. Freq. Control* **65** 300–15
Lockwood G R, Talman J R and Brunke S S 1998 Real-time 3D ultrasound imaging using sparse synthetic aperture beamforming *IEEE Trans. Ultrason. Ferroelectr. Freq. Control* **45** 980–8
Lorintiu O, Liebgott H, Alessandrini M, Bernard O and Friboulet D 2015 Compressed sensing reconstruction of 3D ultrasound data using dictionary learning and line-wise subsampling *IEEE Trans. Med. Imaging* **34** 2467–77
Lustig M, Donoho D and Pauly J M 2007 Sparse MRI: the application of compressed sensing for rapid MR imaging *Magn. Reson. Med.* **58** 1182–95
Misaridis T and Jensen J A 2005 Use of modulated excitation signals in medical ultrasound. Part III: High frame rate imaging *IEEE Trans. Ultrason. Ferroelectr. Freq. Control* **52** 208–19
Ortega A, Provost J, Tong L, Santos P, Heyde B, Pernot M and D'hooge J 2016 A comparison of the performance of different multiline transmit setups for fast volumetric cardiac ultrasound *IEEE Trans. Ultrason. Ferroelectr. Freq. Control* **63** 2082–91
Papadacci C, Bunting E A and Konofagou E E 2017a 3D quasi-static ultrasound elastography with plane wave *in vivo IEEE Trans. Med. Imaging* **36** 357–65
Papadacci C, Bunting E A, Wan E Y, Nauleau P and Konofagou E E 2017b 3D myocardial elastography *in vivo IEEE Trans. Med. Imaging* **36** 618–27
Papadacci C, Pernot M, Couade M, Fink M and Tanter M 2014 High-contrast ultrafast imaging of the heart *IEEE Trans. Ultrason. Ferroelectr. Freq. Control* **61** 288–301
Peng S-Y and Li M-L 2015 Linear array beamformation using virtual sub-wavelength receiving elements *Presented at the Ultrasonics Symp. (IUS), 2015 IEEE Int.* pp 1–4
Petrusca L, Varray F, Souchon R, Bernard A, Chapelon J Y, Liebgott H, N'Djin W A and Viallon M 2018 Fast volumetric ultrasound B-mode and Doppler imaging with a new high-channels density platform for advanced 4D cardiac imaging/therapy *Appl. Sci.* **8** 200
Ponnle A, Hasegawa H and Kanai H 2013 Suppression of grating lobe artifacts in ultrasound images formed from diverging transmitting beams by modulation of receiving beams *Ultrasound Med. Biol.* **39** 681–91
Provost J, Papadacci C, Arango J E, Imbault M, Fink M, Gennisson J L, Tanter M and Pernot M 2014 3D ultrafast ultrasound imaging *in vivo Phys. Med. Biol.* **59** L1
Rasmussen M F and Jensen J A 2014 Comparison of 3D synthetic aperture phased-array ultrasound imaging and parallel beamforming *IEEE Trans. Ultrason. Ferroelectr. Freq. Control* **61** 1638–50
Salgo I S 2007 Three-dimensional echocardiographic technology *Cardiol. Clin.* **25** 231–9
Tiran E, Deffieux T, Correia M, Maresca D, Osmanski B F, Sieu L A, Bergel A, Cohen I, Pernot M and Tanter M 2015 Multiplane wave imaging increases signal-to-noise ratio in ultrafast ultrasound imaging *Phys. Med. Biol.* **60** 8549–66
Tong L, Ortega A, Gao H and D'hooge J 2013 Fast three-dimensional ultrasound cardiac imaging using multi-transmit beam forming: a simulation study *Presented at the Ultrasonics Symp. (IUS), 2013 IEEE Int.* pp 1456–9
Torbatian Z, Adamson R and Brown J A 2013 Experimental verification of pulse-probing technique for improving phase coherence grating lobe suppression *IEEE Trans. Ultrason. Ferroelectr. Freq. Control* **60** 1324–32
Torbatian Z, Adamson R, Bance M and Brown J A 2010 A split-aperture transmit beamforming technique with phase coherence grating lobe suppression *IEEE Trans. Ultrason. Ferroelectr. Freq. Control* **57** 2588–95
Turnbull D H and Foster F S 1991 Beam steering with pulsed two-dimensional transducer arrays *IEEE Trans. Ultrason. Ferroelectr. Freq. Control* **38** 320–33
Van den Berg E and Friedlander M P 2007 SPGL1: a solver for large-scale sparse reconstruction *Linear Algebra and Optimization Seminar* (Stanford University, 17 October 2007) (Online: www.cs.ubc.ca/labs/scl/spgl1)
Van den Berg E and Friedlander M P 2008 Probing the Pareto frontier for basis pursuit solutions *SIAM J. Sci. Comput.* **31** 890–912
Varnosfaderani M H H, Asl B M and Faridsoltani S 2018 An adaptive synthetic aperture method applied to ultrasound tissue harmonic imaging *IEEE Trans. Ultrason. Ferroelectr. Freq. Control* **65** 557–69
Wang J and Lu J-Y 2007 Motion artifacts of extended high frame rate imaging *IEEE Trans. Ultrason. Ferroelectr. Freq. Control* **54** 1303–15
Yen J T, Steinberg J P and Smith S W 2000 Sparse 2D array design for real time rectilinear volumetric imaging *IEEE Trans. Ultrason. Ferroelectr. Freq. Control* **47** 93–110